

Experimental and modeling studies of imaging with curvilinear electronic eye cameras

Viktor Malyarchuk,¹ Inhwa Jung,¹ John A. Rogers,^{1,*}
Gunchul Shin,² and Jeong Sook Ha²

¹Department of Materials Science and Engineering, Frederick Seitz Materials Research Laboratory,
University of Illinois at Urbana-Champaign, Urbana, Illinois 61801, USA

²Department of Chemical and Biological Engineering,
Korea University, Seoul 136-701, Korea
*jrogers@illinois.edu

Abstract: Model calculations and the experimental measurements of the imaging properties of planar, hemispherical, and elliptic parabolic electronic eye cameras are compared. Numerical methods for comprehensive full field calculations of image formation are enabled by use computationally efficient modes. Quantitative agreement between these calculations and experimentally measured images of test patterns reveals advantages of curvilinear camera systems, and provides guidelines for future designs.

©2010 Optical Society of America

OCIS codes: (080.1753) Computation methods; (080.2740) Geometric optical design.

References and links

1. L. P. Lee, and R. Szema, "Inspirations from biological optics for advanced photonic systems," *Science* **310**(5751), 1148–1150 (2005).
2. S.-B. Rim, P. B. Catrysse, R. Dinyari, K. Huang, and P. Peumans, "The optical advantages of curved focal plane arrays," *Opt. Express* **16**(7), 4965–4971 (2008).
3. H. C. Ko, M. P. Stoykovich, J. Song, V. Malyarchuk, W. M. Choi, C.-J. Yu, J. B. Geddes 3rd, J. Xiao, S. Wang, Y. Huang, and J. A. Rogers, "A hemispherical electronic eye camera based on compressible silicon optoelectronics," *Nature* **454**(7205), 748–753 (2008).
4. I. Jung, G. Shin, V. Malyarchuk, J. S. Ha, and J. A. Rogers, "Paraboloid electronic eye cameras using deformable arrays of photodetectors in hexagonal mesh layouts," *Appl. Phys. Lett.* **96**(2), 021110 (2010).
5. A. Walthers, *The Ray and Wave Theory of Lenses*, (Cambridge Univ. Press, Cambridge, UK, 1995).
6. M. Born, and E. Wolf, *Principles of Optics*, 7th edition (Cambridge Univ. Press, New York, 1999)
7. G. H. Spencer, and M. V. R. K. Murty, "General Ray-Tracing Procedure," *J. Opt. Soc. Am.* **52**(6), 672–678 (1962).
8. E. Hecht, *Optics*, (Addison Wesley, 2002)
9. CODE V, Optical Research Associates, East Foothill Boulevard, Pasadena, CA 91107.
10. ZEMAX, ZEMAX Development Corporation, 3001 112th Avenue NE, Suite 202, Bellevue, WA 98004.
11. B. Gustavsson, "Optical_bench", <http://www.mathworks.com/matlabcentral/fileexchange/27412-opticalbench>.
12. G. Shin, I. Jung, V. Malyarchuk, J. Song, S. Wang, H. C. Ko, Y. Huang, J. S. Ha, and J. A. Rogers, "Micromechanics and advanced designs for curved photodetector arrays in hemispherical electronic-eye cameras," *Small* **6**(7), 851–856 (2010).
13. H. Ojanen, "Undistort", <http://www.math.rutgers.edu/~ojanen/undistort>.

1. Introduction

Design options for modern digital cameras are restricted by the use of planar detectors, which require the image (Petzval) surfaces to be flat. Typically, multi-lens arrangements are needed to achieve this outcome. The complexity of the resulting optical systems contrasts with the comparative simplicity of those in most biological systems [1]. Achieving such results can be accomplished by adding curvature to the detector, to match that of images formed with simple lenses. Replacing a planar detector with a curved system in a man-made camera could achieve the same level of simplicity, thereby offering opportunities to reduce the size, cost and weight of the lenses [2–4]. Use of an elliptic paraboloid detector can match very closely the Petzval surface associated with the simplest optical system, i.e. a single spherical lens. Alternatively, detector shape could be used in combination with lens design to achieve any desired balance of various system parameters.

The imaging performance of commercially available detectors can be analyzed by means of geometrical optics. The classical approach uses numerical ray tracing [5–8]. Despite its simplicity, where only Snell's law is used for transparent systems, full imaging analysis in this manner can be challenging due to a large number of propagating beams needed for reconstruction. To obtain photographic quality images with low noise levels, every illuminated point of the object must be modeled explicitly. Monte-Carlo algorithms are often employed for such calculations [9,10]. Previous analysis of curvilinear imaging systems relied on consideration of a relatively small number of principal rays [2]. Although such an approach enables fast computation, the results obtained by this method can vary with number of beams, eventually converging to an exact solution.

Here, we identify approaches that enable full field simulations, with near photographic quality, where more than 20 billion beams can be included explicitly. The method exploits the cylindrical symmetry of optical systems built with spherical lenses. Assuming that the object is a square consisting of N points along every axis, the number of points necessary for the ray tracing can be reduced from N^2 to $\sim N$. Such approaches, implemented in computationally efficient modes, allow detailed, quantitative study of experimentally measured imaging characteristics associated with curvilinear detectors. Precise agreement between modeling and experiment for the cases of planar, hemispherical, and elliptic parabolic electronic eye cameras, confirms the validity of our numerical methods and provides insights into the imaging properties.

2. Model and experimental setup

Figure 1 shows a schematic illustration of the particular optical setup that forms the focus of our work. A single plano-convex lens (CPX10093/000 from JML Optical Industries, Inc.; diameter = 9 mm, focal length = 22.8 mm) mounts 67 mm away from the diffused area of an light emitting diode based backlight (MB-BL4X4-W-24 from Metaphase Technologies, Inc.). This backlight provides uniform, white light illumination of mounted objects, consisting here of a transparency mask with a pattern of transparent dots on an opaque background. The lens holder provides two apertures in the system. The first, with a diameter of 9.25 mm, lies at a distance of 0.4 mm from the convex surface of the lens (facing object). The second has a diameter of 8.4 mm, and is 3.1 mm away from planar lens surface (facing screen). The object (transparency film) lies at the position -67 mm in Fig. 1. The object and the apertures do not appear in this schematic diagram, but they are taken into account in the analytical model. The rays in Fig. 1 were defined using an open source ray tracing tool (Optical_bench [11]). The curvature of the image surface is evident from these rays; hemispherical (blue) and elliptic paraboloid (green) screens depicted in Fig. 1 show approximations to this curvature. A planar (red) screen and apices of the parabolic and hemispherical surfaces are located at the position of best focus (34 mm) at the center of the image. The ideal (paraboloid) surface was determined by evaluating the shift of this position of best focus from the center of the image toward its edges.

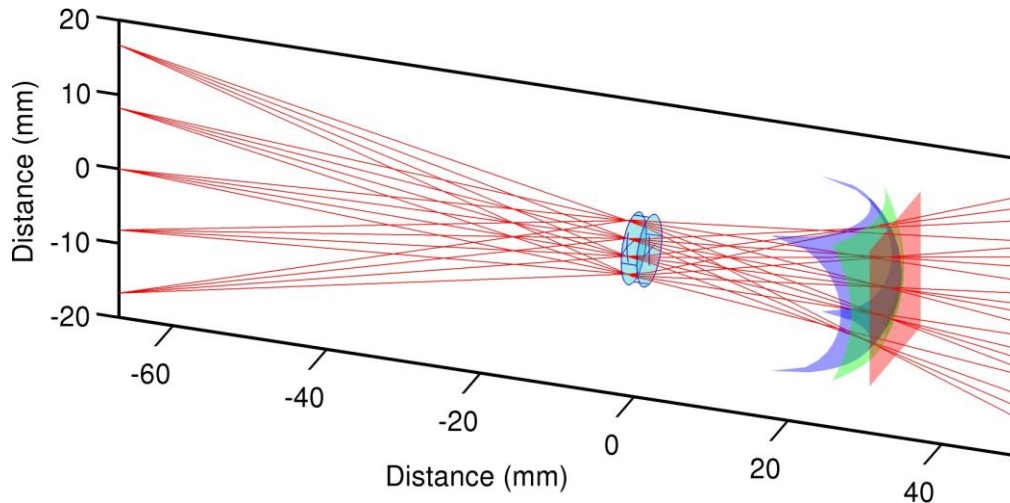


Fig. 1. Schematic illustration of the experimental setup. The object (not shown) mounts on a backlight at the position of -67 mm. A lens holder (not shown) and a 9 mm diameter plano-convex lens are located at 0 mm. The convex surface of the lens faces the object; the planar surface faces the screen. Planar (red), elliptic paraboloid (green) and hemispherical (blue) screens are shown. The planar detector and the apices of parabolic and spherical detectors are at the position best focus for the center of the field of view, i.e. 34 mm.

3. Numerical procedures

To simulate images produced by this optical system, it is necessary to perform ray tracing at every point of the object. Assuming the object is a square with a size of $N \times N$, where N is the number of points along each axis, N^2 points should be analyzed. However, this number can be greatly reduced by exploiting the symmetry of the system. In particular, the cylindrical geometry allows calculation at a limited subset of points, such that these results can be reused for equivalent locations in other parts of the image. For a flat object normal to the optical axis, all points at the same distance from the axis can be considered as the same. There are $\sim N$ such points. Final images can be rendered by combining such simulation results.

3.1 Obtaining point spread functions

The first stage of the image simulation is to build a model with Optical_bench [11] that matches the experimental setup described in the introduction. The full object geometry is not considered at this stage. Due to the cylindrical symmetry, the first pixel lies at the center of the object, such that beams originating from this location strike the center of the lens at the optical axis. The last point is at the corner of the square screen. For the geometry of Fig. 1, beams originating from this point strike the lens at an angle of 46.6° away from the optical axis. All other computed points lie on the line connecting the first and the last ones; for calculations presented here, we used an angular step of 0.01° .

Fans of 10,000 rays emerging from each point on the object are propagated through the lens and the corresponding apertures. Beams are distributed in equidistant fashion over the entire range of angles to fill the front aperture with light originating from the center of the object. The angles remain the same for all other points, to keep the illumination consistent. A large number of beams fall on the image screen to form a spot of light that represents the system response to a point light source, i.e., the point spread function (PSF).

Since every point is independent, the full process can be parallelized, with each pixel assigned to its own processor. Such a parallel process gives a set of PSFs for every point of interest and for every screen position used in the model. The flowchart that describes this procedure for generating PSFs appears in Fig. 2.

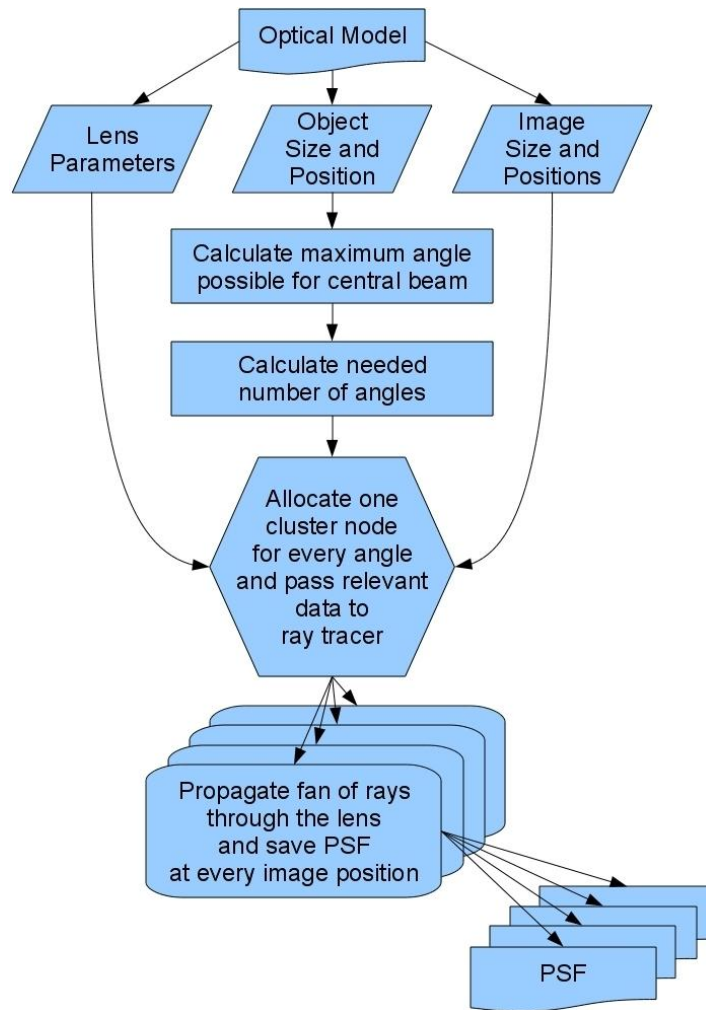


Fig. 2. Flowchart for the process used to generate point spread functions, in a parallel fashion.

3.2 Rendering of the object

Every point of the object is imaged as a PSF on the screen. To simulate the final image at a particular position on the screen, it is necessary to add PSFs for the corresponding point. To accomplish this computation, relevant PSFs are chosen from the set calculated in subsection 3.1. Before adding each PSF to the screen, it is rotated to the proper polar angle and normalized by the intensity of the corresponding point at the object plane. The intensity is also corrected, assuming that the object surface is Lambertian. Such a simulation procedure can be accelerated further by rendering every line of the object in parallel as shown in Fig. 3.

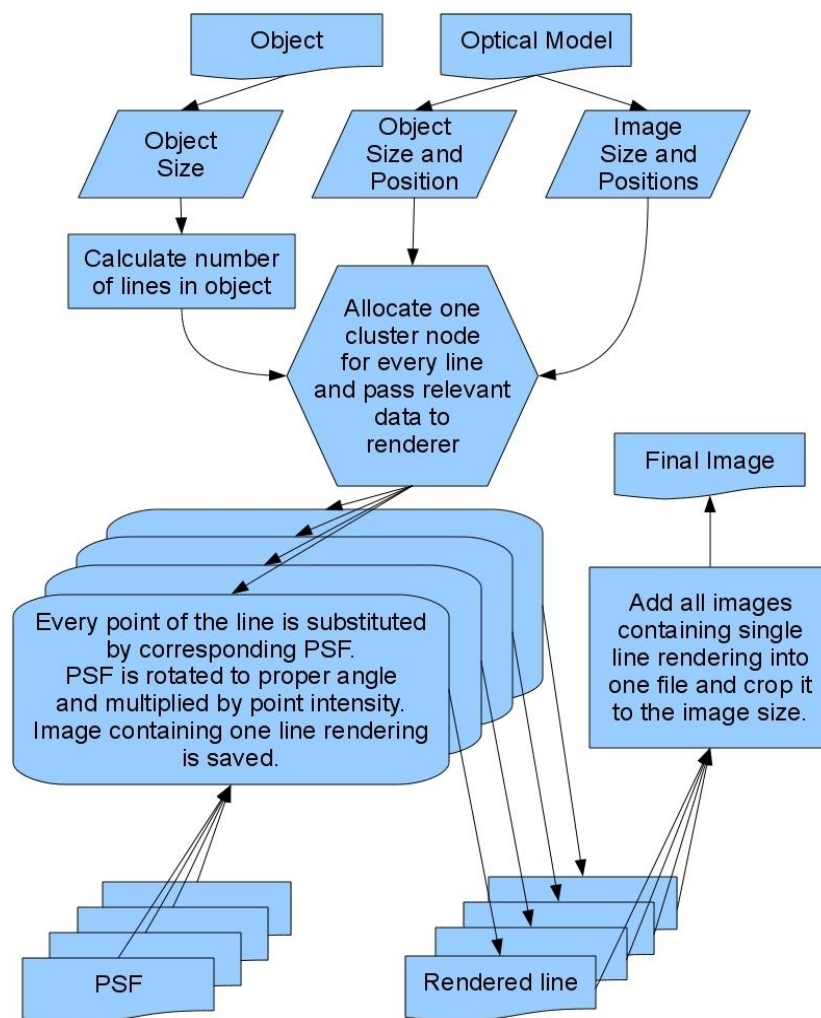


Fig. 3. Flowchart for the process used to render images, in a parallel fashion.

4. Modeling and experimental results

Utilizing numerical procedures described in section 3, it is possible to build high resolution images at different screen positions around the focal plane. PSFs obtained by ray tracing can be used as tools for optimizing and analyzing the optical system.

4.1 Analysis of point spread function

The quality of images can be estimated by examining the shape of the PSFs. Point-like PSFs represent the perfectly focused state; deviations induce broadening and distortions in the images. Defocusing dominates at the center of the screen, as is clearly observable in Figs. 4–6 at the zero position of the vertical axis. PSFs near the screen edge exhibit coma aberrations or astigmatism, or both in some cases.

Figure 4 shows a set of representative PSFs for the case of a planar screen. The point at the origin (0 mm in distance) for the uppermost PSF corresponds to the center on the object surface. The central beam is at the axis of the optical system. Every next PSF originates from the object's location where the central ray is 2° apart from the previous one. The vertical axis is measured in distance from the center (0 mm) of the screen. The horizontal axis is the position of the screen on the optical axis of the system as defined in Fig. 1. The screen

position with best focus at its center is 34 mm from the lens. Intensities are normalized for clarity.

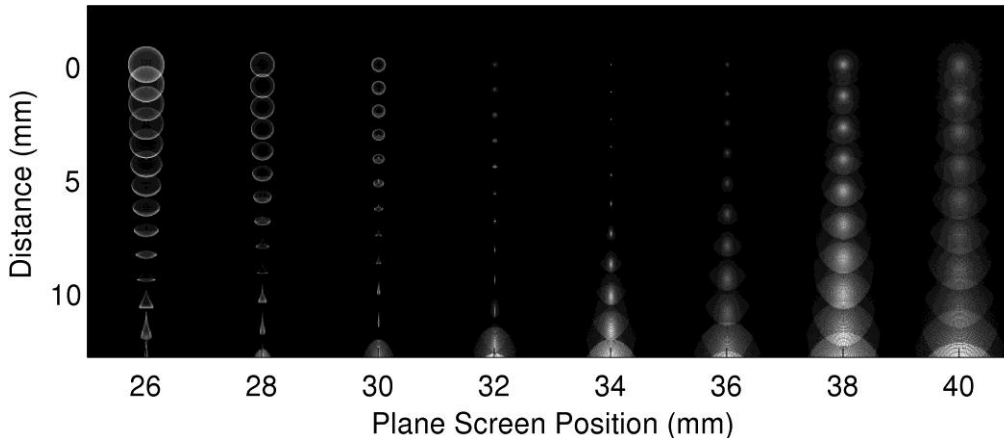


Fig. 4. Representative point spread functions for the planar detector screen. The vertical axis shows the distance from the center of the screen. The center of screen is defined as 0 mm. The horizontal axis shows the distance from the lens. Best focus at the center of the screen occurs at 34 mm. Points of origin for the PSFs are in the object plane at its center for the 0 mm row. The central ray is along the axis of the optical system. Consecutive PSFs are obtained from the points apart from each other by 2° .

The results show clearly that defocusing is significant at any screen position beyond 34 mm (data at 36, 38 and 40 mm are shown in Fig. 4). Screens positioned too close to the lens (26, 28 and 30 mm) also do not deliver focused images. As with large distances, the PSFs show both out of focus effects as well as astigmatism and coma aberrations. The evolution of PSFs formed at the center of the screen toward its edge at 32 and 34 mm clearly illustrates limiting features of flat detectors, for this simple imaging system. Although excellent focus obtains at the center of the screen at 34 mm, the PSFs quickly degrade with distance toward the edge of the detector. Similar trends are observed for the screen positioned at 32 mm, but in this case the best focus occurs roughly halfway between the center and the edge; the extent of defocusing increases from this position toward both the edge and the center.

Replacing a flat screen with a hemispherical one dramatically improves the quality of the PSFs. Here, point-like shapes are observed over a much larger area of the detector when positioned at the best focal point, i.e. at 34 mm as shown in Fig. 5. Even with this geometry, however, the PSFs broaden toward the edge of screen. Comparison of PSFs at 34, 36 and 38 mm columns in Fig. 5 suggests the possibility for further optimization. In particular, although there are no point-like PSFs at 36 and 38 mm, those located near the edge are more compact, which implies the ability to improve the quality of the image with a refined curvilinear shape.

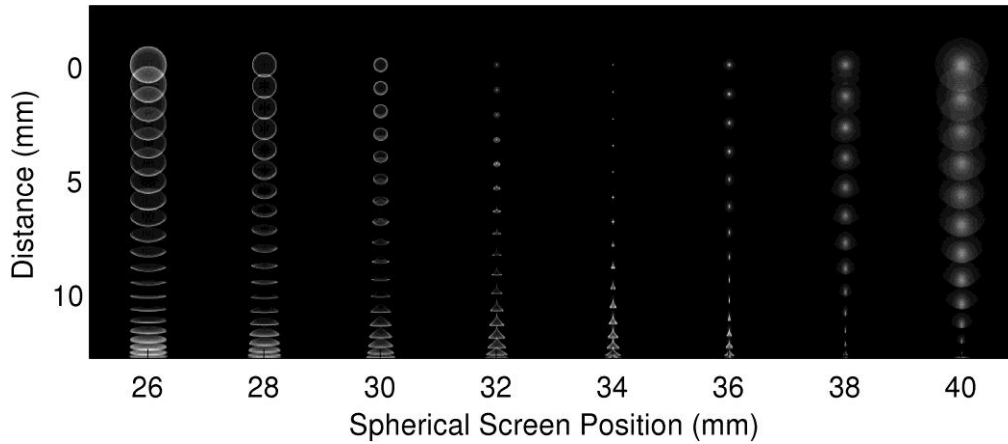


Fig. 5. Representative point spread functions for the hemispherical detector screen. The data represent projections of PSFs on a hemisphere onto a flat surface.

PSFs for the parabolic detector, with a shape that is close to the ideal, appear in Fig. 6. When the detector is positioned at the distance of best focus (34 mm), point-like PSFs obtain for most of the surface area of the screen. Small comma aberrations become noticeable at the edges. Such effects can be corrected by introducing a small aperture at the center of the lens.

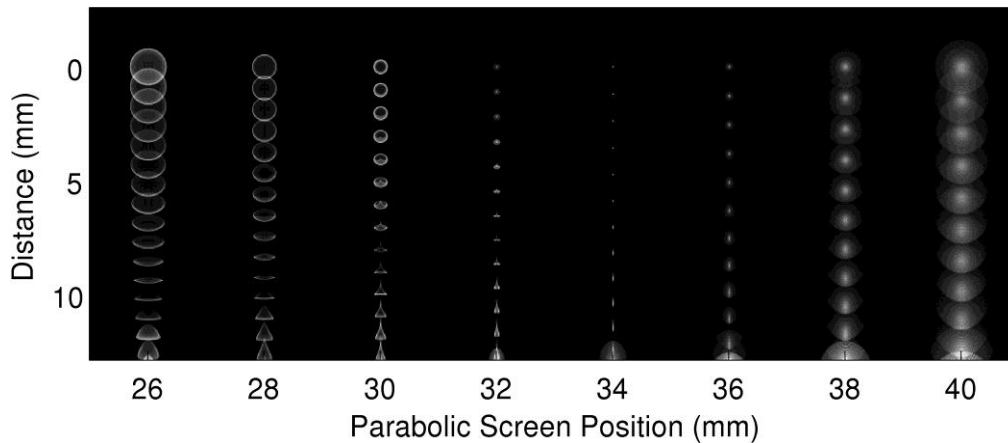


Fig. 6. Representative point spread functions for a parabolic detector screen. The data represent projections of PSFs on a paraboloid onto a flat surface.

The sizes of the PSFs at each screen position are similar to each other, regardless of distance from the center of the screen, as shown in Fig. 6. This observation suggests that the defocusing effect is uniform over all parts of the detector. Images are well focused over the whole area when the detector lies at the focal point of the lens, which is different than the behavior for flat and hemispherical detectors.

4.2 Parameters for hemisphere and elliptic paraboloid surfaces

Parameters of the elliptic paraboloid matched to the image surface were deduced by propagating beams through the system as described in subsection 3.1. A set of planar screens were positioned at distances between 25 and 35 mm with a step of 0.1 mm. Fans of rays originating from a single point on the object surface produced PSFs for all screens. Coordinates of the best focus were chosen as the pixel with maximum intensity on the screen, where the PSF shows the maximum intensity as well. In this way, a set of points originating from the center of the object to its edge produces an array of best focus coordinates. Fitting

these data yielded parameters required for the elliptic paraboloid, where the curvature is given by $Y = 34 - 0.029 X^2$.

The radius of curvature (12.9 mm) for the hemisphere was chosen to match the curvilinear electronic eye camera used in experiment [3].

4.3 Flat screen

Experimental and modeling results for the flat detector appear in Fig. 7. The experiments used a flat, thin film screen made from piece of non developed photographic film. Commercial digital photo camera was used to take images projected on the screen. A band pass filter ($\lambda = 560 \pm 30$ nm) was installed in front of the lens to reduce chromatic

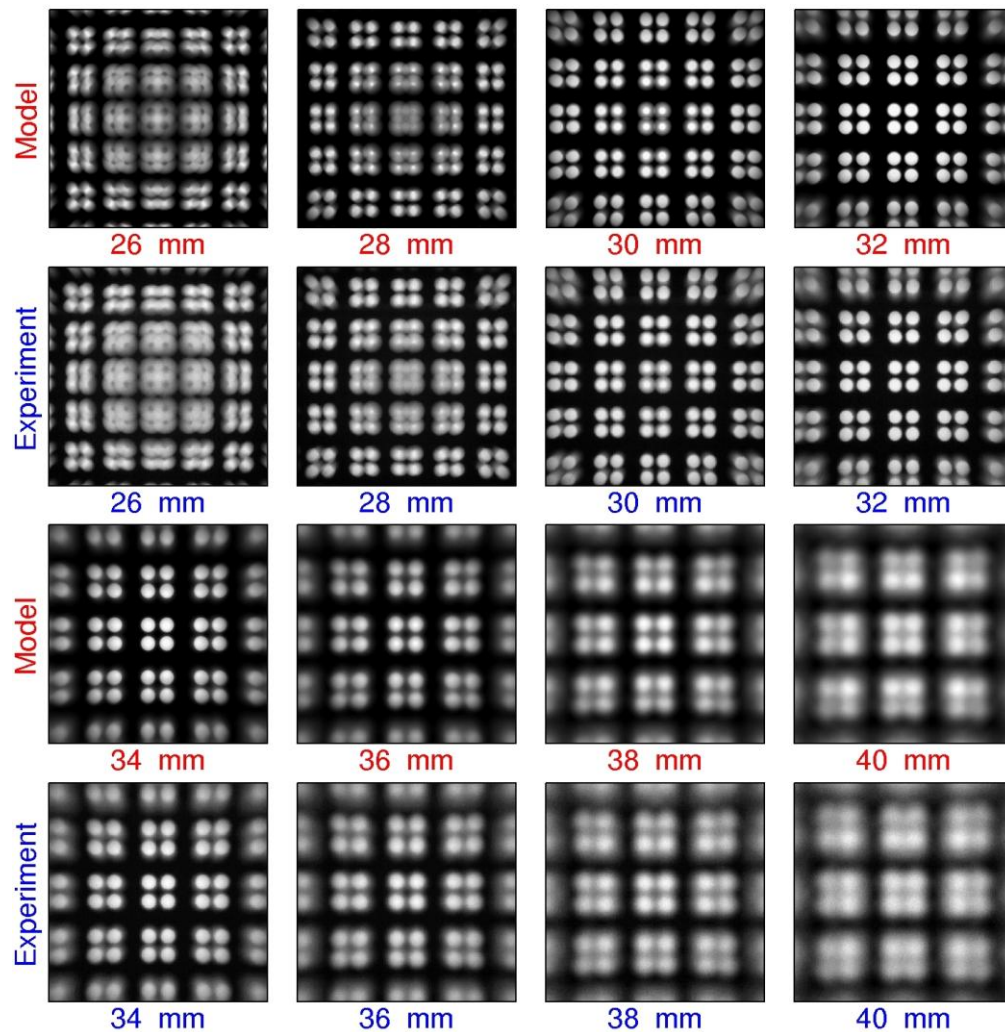


Fig. 7. Comparison of modeling results and experimental images for planar detectors. Odd and even rows show modeling and experimental results, respectively, for different detector positions. 34 mm is the position of the best focus in the middle of the screen.

aberrations. The same wavelength (560 nm) was used in simulations. Odd and even rows correspond to simulations and experimental measurements, respectively. The first and the second rows show the results obtained by using the detectors positioned at distances between

26 and 32 mm with a step of 2 mm. The third and the fourth are between 34 and 40 mm with the same step.

The results show almost perfect correspondence between experiment and modeling. Very slight discrepancies can be attributed to the fact that simulation results are monochromatic but experimental ones are not. Excellent agreement between simulation and experiment for the flat case confirms the validity of the modeling and its extension to the hemispherical and paraboloid cameras.

4.4 Hemispherical screen and electronic eye camera

Figure 8 compares images obtained by simulation, and two types of experiments: one that used a hemispherical screen and digital camera, and another that used a hemispherical electronic eye (e-eye) camera reported previously [3,12]. The hemispherical screen consists of a 1 mm thin transparent polystyrene shell containing a layer of light scattering material (white spay paint).

First and fourth rows of Fig. 8 correspond to simulations; the second and fifth are experimental measurements with hemispherical screen; the third and sixth are data collected with e-eye camera. Rows one, two and three show results obtained using detectors positioned at distances between 26 and 32 mm with a step of 2 mm. Rows four, five and six are between 34 and 40 mm with the same step. Every image corresponds to a projection from the hemispherical surface onto a planar one.

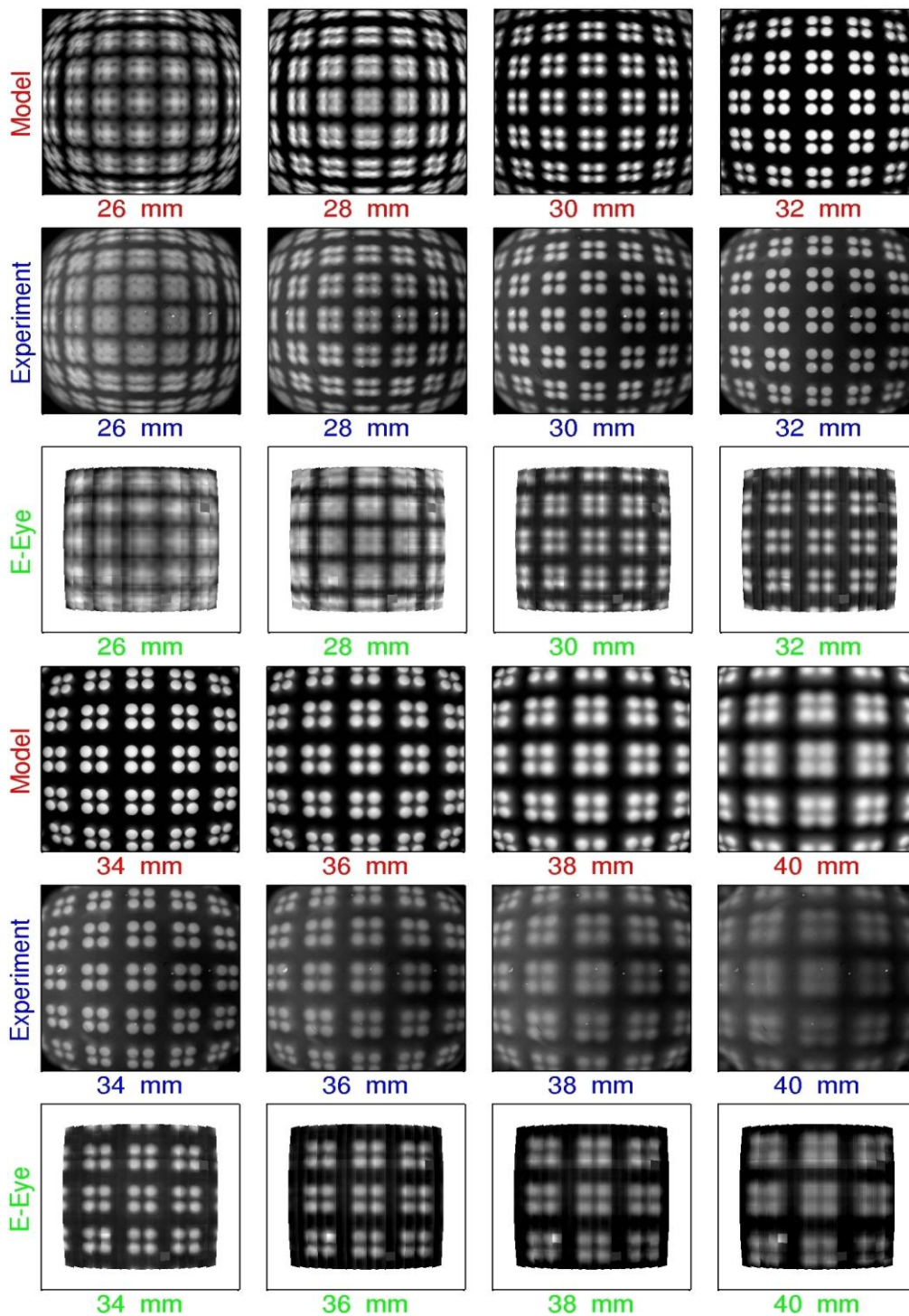


Fig. 8. Comparison of modeling images with experimental ones by using hemispherical screens. First and fourth rows show modeling. Second and fifth show experimental results. Third and sixth are images collected with a hemispherical camera (e-eye). 34 mm is the position of the best focus. Images correspond to projections from the hemispherical surface onto a planar one.

Modeling and experimental results from the hemispherical screen show quantitative agreement, and imaging features that are consistent with expectation based on the behavior of the PSFs. The experimental resolution of e-eye camera is limited by the size of individual pixels ($520 \times 520 \mu\text{m}^2$). Convoluting the simulated images with a similarly sized aperture yields a perfect match in this case as well (not shown here).

4.5 Elliptic paraboloid

Figure 9 shows modeling and experimental results for an elliptic paraboloid detector. The layout and the scales are the same as those used in Fig. 7. The experiments used a screen similar to the one for the hemispherical case, but with a shape that matches the optimal paraboloid surface determined in subsection 4.2. The results show that this paraboloid case yields the best images: at the detector position of the best focus, i.e. 34 mm, all the spots have a uniform shape and intensity.

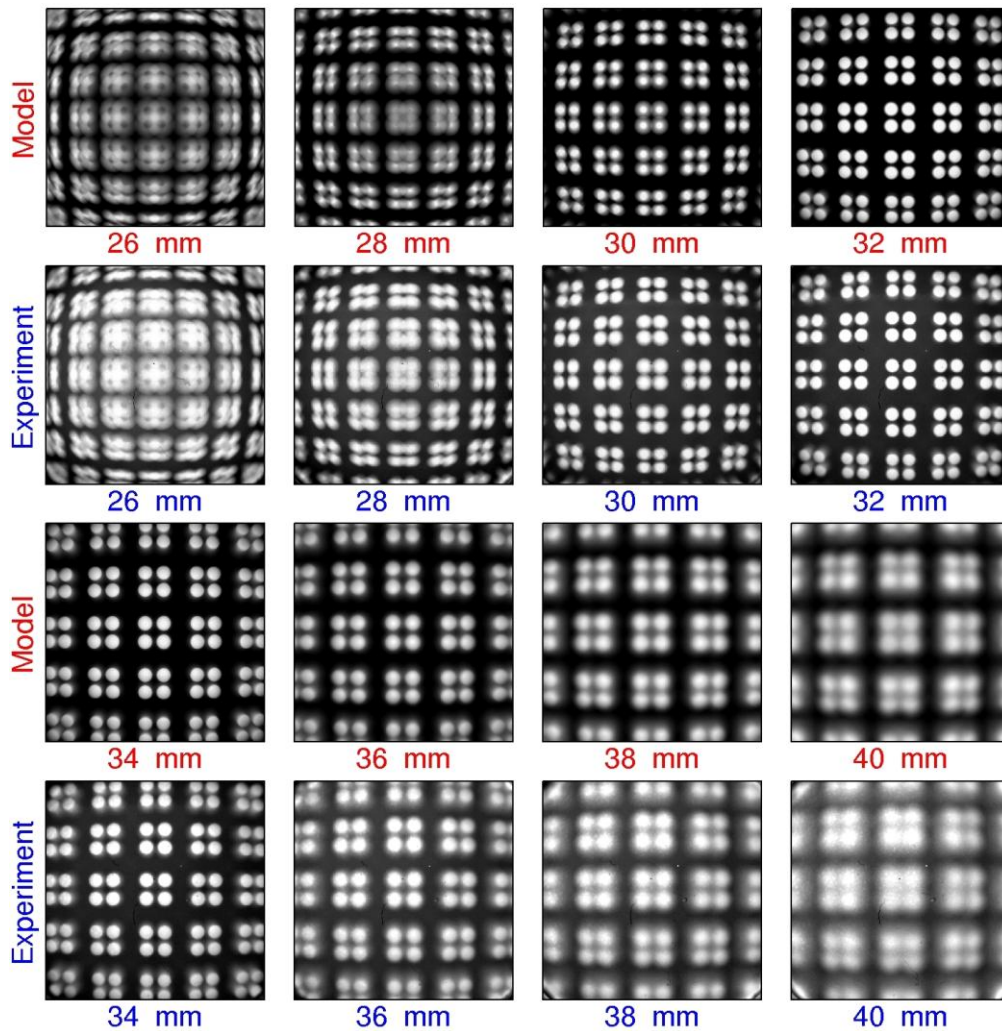


Fig. 9. Comparison of modeling with experimental images taken by paraboloid screens. Odd and even rows show modeling and experimental results, respectively with variation of the detector position. 34 mm is the position of the best focus. Images correspond to projections from the elliptic paraboloid surface onto a planar one.

4.6 Pixel size normalization

For comparison, we assume that all photodetectors in the flat or curvilinear cases are the same size. For the purpose of modeling, curvilinear screens are constructed from individual pixels of different size, with planar projections that are the same size. Pixels which deviate strongly from the projected plane are, as a consequence, bigger than others. Radiometrically correct simulations are possible, however, through pixel size normalization. Numerical integration was employed to calculate the size of the each pixel in hemispherical and elliptical paraboloid screens. Correction coefficients were obtained by normalizing the pixel size by the size of the smallest pixel. Figure 10 shows such coefficients for non-planar screens considered here. Normalized results are obtained by dividing the light collected by every pixel by the corresponding correction coefficient. Such compensation is included all simulations presented Figs. 8 and 9.

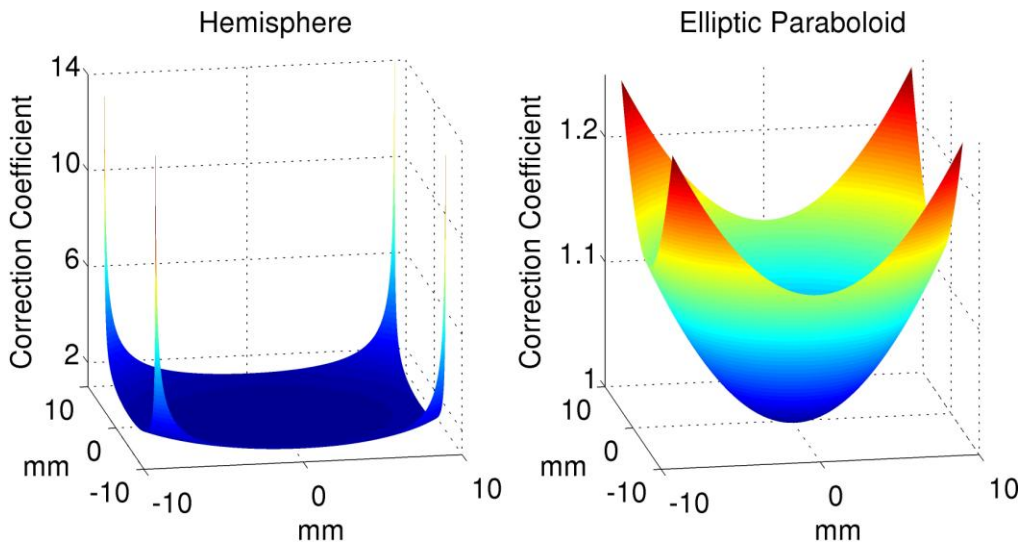


Fig. 10. Correction coefficients for amount of radiation collected by hemispherical and elliptical paraboloid screens.

4.7 Distortion correction

While hemispherical and elliptic paraboloid detectors deliver significant improvement in image quality over planar ones, they also introduce a noticeable amount of geometric distortion, if projected simply onto a flat surface. These distortions are clearly visible in Fig. 7–9. This problem is well known to manufacturers of low cost single lens digital cameras; it is routinely corrected in their firmware [13]. Examples of such distortion compensation for cases considered here are shown in Fig. 11.

Regular dots pattern were simulated for each case considered here. Coordinates of the centers of the dots were extracted and compared to the case of an ideal pinhole camera. Mismatch between the two cases yield a set of distortion compensation parameters. This set is used to extrapolate correction parameters for any point of the image. Part of the distortion that is introduced by the planar projection used here; this component cannot be completely compensated by correcting the projection only. For this reason, some residual distortion remains in the corners for the non-planar screens. Polar projects can avoid this limitation.

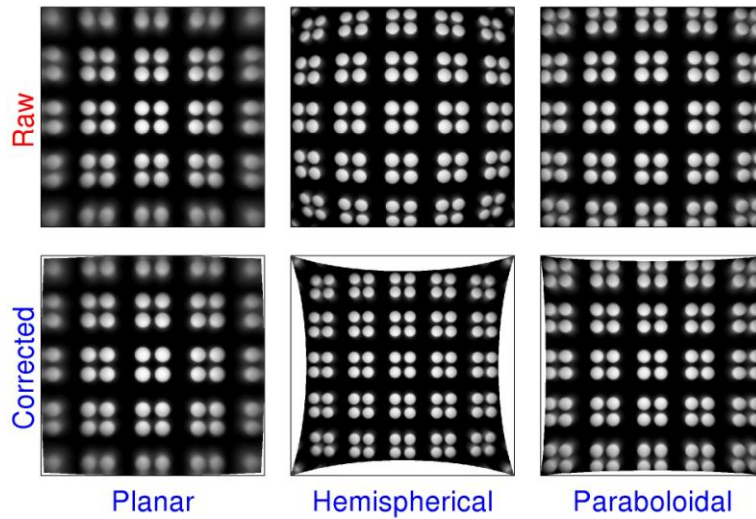


Fig. 11. Distortion correction for planar hemispherical and elliptic paraboloid cases. Images correspond to projections from the curvilinear surface onto a planar one.

5. Conclusion

Optical properties of planar, hemispherical and rotational paraboloid detectors have been investigated via efficient numerical methods that also exploit the cylindrical symmetry of the system, to allow comprehensive analysis. The numerical results show nearly perfect agreement with experimental results for all cases examined. The results demonstrate the utility of these simulation tools, for investigating the properties of curvilinear imaging devices, with the potential to facilitate future work on these or related systems.

Acknowledgements

All the experiments were carried out in the Frederick Seitz Materials Research Laboratory Central Facilities, University of Illinois, partially supported by the U.S. Department of Energy under grants DE-FG02-07ER46453 and DE-FG02-07ER46471. G.S. and J. S. H. acknowledge Korea Science and Engineering Foundation (KOSEF) through the National Research Lab. Program funded by the Ministry of Science and Technology (No. ROA-2007-000-20102-0).